

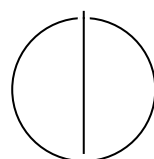
SCHOOL OF COMPUTATION,
INFORMATION AND TECHNOLOGY —
INFORMATICS

TECHNISCHE UNIVERSITÄT MÜNCHEN

Master's Thesis in Informatics

**Design and Control of an Aerodynamic
Surface-Enhanced Multirotor**

William Constantin Rosenhahn





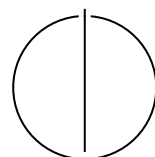
SCHOOL OF COMPUTATION,
INFORMATION AND TECHNOLOGY —
INFORMATICS

TECHNISCHE UNIVERSITÄT MÜNCHEN

Master's Thesis in Informatics

**Design and Control of an Aerodynamic
Surface-Enhanced Multirotor**

Author: William Constantin Rosenhahn
Examiner: Prof. Dr.-Ing. Markus Ryll
Supervisor: Lukas Pries
Submission Date: 01.12.2025



I confirm that this master's thesis is my own work and I have documented all sources and material used.

Munich, 01.12.2025

William Constantin Rosenhahn

Acknowledgments

Abstract

Contents

Acknowledgments	iii
Abstract	iv
1 Introduction	1
1.1 Motivation	1
1.2 Problem statement and scope	1
1.3 Contributions	1
1.4 Thesis organization	2
2 Background	3
2.1 Aerial vehicle classes	3
2.2 Rigid-body frames and notation	3
2.3 Aerodynamic preliminaries	3
3 Related Work	4
3.1 Baselines: Agility vs. Efficiency	4
3.2 Controller Classes Used Across the Spectrum	5
3.3 Aerodynamic Augmentation on Multicopters	5
3.4 Shrouds and Ducts as Augmentation	6
3.5 Quantitative Comparison Across Criteria	7
3.6 Gaps and Open Issues	7
3.7 Why a Quadrotor with Fixed Aerodynamic Surfaces?	8
4 Dynamics Model	9
4.1 Coordinate Frames and States	9
4.2 Forces	9
4.2.1 Gravity	10
4.2.2 Rotor Thrust	10
4.2.3 Aerodynamic Forces	10
4.3 Moments	10
4.4 Equations of Motion	11
4.5 Assumptions and Simplifications	11

Contents

4.6 Remarks	11
5 Platform Design	12
5.1 Platform Design	12
5.1.1 Configuration and Layout	12
5.1.2 Wing Aerodynamics	13
5.1.3 Propulsion and Actuation	15
6 Control Architecture	17
6.1 Reference Generation	17
6.2 Geometric Outer Loop	17
6.2.1 Translational feedback and force target	18
6.2.2 Attitude target and thrust projection	18
6.2.3 Tilt-prioritized attitude control and rate reference	19
6.3 INDI Inner Loop	19
6.3.1 Measured/filtered quantities	19
6.3.2 Nominal NDI versus incremental INDI moments	20
6.3.3 Update to rotor thrusts	20
6.4 Control Allocation and Constraints	21
6.5 Implementation Notes	21
6.6 Tuning Guidance	21
6.7 Summary	22
7 Experimental Setup	23
7.1 Experimental Setup	23
7.1.1 Hardware	23
7.1.2 Software	27
7.1.3 Facilities	28
8 Experiments and Evaluation	30
8.1 Thrust map identification	30
8.2 Agility and tracking	30
8.3 Aerodynamic forces/moment quantification	32
8.4 Efficiency assessment	32
8.5 Baseline comparison	32
9 Conclusion	33
Abbreviations	34

Contents

List of Figures	35
List of Tables	36
Bibliography	37

1 Introduction

1.1 Motivation

Micro air vehicles (MAVs) with efficient autonomous navigation can strengthen applications such as search-and-rescue and last-mile delivery, where safety, robustness, and endurance are critical. Conventional quadrotors offer agility and precise control but are power-inefficient in sustained forward flight. Fixed-wing platforms are efficient but cannot hover and are less maneuverable in confined spaces. Hybrid vertical take-off and landing (VTOL) concepts improve mission versatility but increase mechanical and control complexity. This thesis investigates an intermediate design: a multirotor augmented with fixed aerodynamic surfaces to harvest passive lift during horizontal motion while keeping multirotor agility.

1.2 Problem statement and scope

In the presence of aerodynamic surfaces, hard-to-model aerodynamic forces become significant and challenge controller design. We aim to develop a platform and control strategy that:

- preserves quadrotor agility while improving forward-flight efficiency via passive lift,
- tracks agile trajectories accurately without requiring aerodynamic parameter identification, and
- remains robust to modeling errors and disturbances.

The central question is whether an Incremental Nonlinear Dynamic Inversion (INDI)-based controller can achieve accurate trajectory tracking on an aerodynamic surface-enhanced quadrotor without an explicit aerodynamic model.

1.3 Contributions

This thesis presents:

- a design of an aerodynamic surface-enhanced quadrotor in X-wing configuration,
- a dynamics model combining a standard quadrotor 6-DoF model with simplified quadratic lift/drag,
- a trajectory-tracking controller based on geometric control and INDI, including a coordinated-turn option, and
- an experimental evaluation: thrust-map identification, agility/controllability, aerodynamic disturbance characterization, and efficiency assessment.

1.4 Thesis organization

Chapter 3 reviews related work and motivates the chosen design. Chapter 4 derives the model. Chapter 5 details the platform. Chapter 6 presents the controller. Chapters 7 and 8 describe the setup and experiments. Chapter 9 concludes.

2 Background

This chapter introduces foundational concepts relevant to agile and efficient autonomous flight with aerodynamic surface-enhanced multirotors. It briefly covers flight vehicle classes, 6-DoF rigid-body kinematics and dynamics, and aerodynamic fundamentals (lift, drag, moments) used later in the modeling and control chapters.

2.1 Aerial vehicle classes

We distinguish multirotors, fixed-wing aircraft, tailsitters, and general VTOL hybrids. Key trade-offs include agility, efficiency, range, and controllability. Hybrids aim to combine vertical take-off and landing with efficient forward flight.

2.2 Rigid-body frames and notation

We use an inertial/world frame $\{\mathcal{I}\}$ and a body frame $\{\mathcal{B}\}$. Position $\mathbf{p} \in \mathbb{R}^3$, velocity \mathbf{v} , orientation $R \in SO(3)$, angular velocity $\boldsymbol{\omega} \in \mathbb{R}^3$. Standard hat/vee maps and skew operator $[\cdot]_{\times}$ are adopted.

2.3 Aerodynamic preliminaries

Lift $L = \frac{1}{2}\rho V^2 S C_L(\alpha)$ and drag $D = \frac{1}{2}\rho V^2 S C_D(\alpha)$, with α the angle of attack, reference area S , and air density ρ . For small angles or thin-airfoil approximations, $C_L \approx a_\alpha \alpha$, $C_D \approx C_{D0} + k C_L^2$. These models motivate the simplified quadratic lift/drag used in Chapter 4.

3 Related Work

Designing a UAV that is both agile (e.g., sustained $\geq 3g$ banked turns on meter-scale radii with low tracking error) and energy-efficient (low Wh/km or J/m at cruise), while remaining controllable across hover and forward flight, robust to aerodynamic disturbances, and implementable with moderate complexity, requires weighing trade-offs across canonical configurations: multirotors, fixed-wing, tailsitters, tiltrotors/tilt-wings, and quadplane VTOLs. We additionally review “aerodynamically augmented” multicopters—i.e., quadrotors with fixed lifting surfaces or shrouds—because they can mitigate the multirotor’s forward-flight inefficiency without incurring the full complexity of morphing hybrids.

3.1 Baselines: Agility vs. Efficiency

Pure multirotors Pure multirotors excel in agility and controllability in hover and low-speed flight. State-of-the-art quadrotors routinely track aggressive trajectories at 2–5 g and 40–70 km/h with centimeter-level RMS errors using differential-flatness feedforward plus robust inner loops—often incremental nonlinear dynamic inversion (INDI) [TK18; TK21a; FKa22]. For example, Tal and Karaman report tracking at 12.9 m/s with up to 2.1 g and 6.6 cm RMS error, and explicit robustness to added drag and rope pulls due to INDI’s disturbance-rejection properties [TK18]. Foehn et al.’s Agilicious platform demonstrates up to ~ 5 g and ~ 70 km/h autonomous tracking with modern model-predictive and differential-flatness-based controllers, again emphasizing agility and controllability [FKa22]. However, multirotors are energetically inefficient in forward flight because thrust must be tilted to produce lift and drag grows quickly with speed.

Fixed-wing aircraft By contrast, fixed-wing aircraft achieve much lower J/m at cruise because wings supply lift with high L/D , but they cannot hover.

Hybrids: tailsitters, tiltrotors, and quadplanes Tailsitters and tiltrotor/tilt-wing hybrids attempt to combine both: hover on rotors, then transition to wing-borne flight

for efficiency. Recent tailsitter work shows promising agility and envelope coverage—e.g., Lu et al. report 10–20 m/s trajectories with ~ 2.5 g agile maneuvers using a flatness-based planner and robust tracking [LGa22], and Tal and Karaman demonstrate global trajectory-tracking and agile uncoordinated flight (e.g., sideways/knife-edge) using a global INDI framework [TK21b; TK22]. Tilt-wing/tilt-rotor concepts have matured in modeling and flight-dynamics/transitions (e.g., Daud Filho et al. present dynamic models and simulated transition trajectories for a canard-plus-wing tilt concept) but remain mechanically and algorithmically complex, with challenging cross-couplings during transitions [Da24; MJa22]. Quadplanes (fixed wing + vertical-lift rotors) offer practical VTOL with cruise efficiency; experimental examples (e.g., a tandem-wing quadplane) target long-range VTOL with simpler mechanisms than tilting actuators, though added mass/drag can degrade hover agility and gust robustness [OŁ22].

3.2 Controller Classes Used Across the Spectrum

Geometric SE(3) control established a rigorous foundation for aggressive multirotor tracking with global attitude representations [LLM10] and geometric adaptive variants handle parametric uncertainties [GLL15]. Differential-flatness-based planning/control (e.g., minimum-snap) is ubiquitous for trajectory generation and feedforward tracking [MK11; TK18]. INDI has become a go-to inner-loop choice for robustness to unmodeled aero forces/torques at high speed and in gusts [SCM10; SCC17]. A direct empirical comparison on agile quadrotor flight found that both NMPC and differential-flatness-based controllers benefit markedly ($\approx 78\%$ error reduction) from coupling to an INDI inner loop and drag modeling at speeds up to 20 m/s [Sun+21]. These results are important because the proposed quad-with-wings concept aims to keep a multirotor control stack (differential-flatness/geometric + INDI) while adding lightweight aerodynamics.

3.3 Aerodynamic Augmentation on Multicopters

The most directly relevant evidence comes from micro-to-small UAVs that add fixed lifting surfaces to multirotors:

Wings Dawkins and DeVries integrated wings on a micro-quad and quantified the trade-off: $\sim 35\%$ energy saving in forward flight, but $\sim 45\%$ extra power in hover due to added mass/drag; the wing “pays off” beyond $\sim 3\text{--}5$ m/s depending on angle-of-attack and prop wash interaction [DD18]. They report smoother tracking and reduced pitch

angles at speed, indicating improved controllability in forward flight, but some hover agility penalty.

Xiao et al. designed a “lifting-wing fixed on multirotor” with a decoupled wing mount. On a 1.2 kg quad, they measured 50.14% less electrical power at 15 m/s compared with the bare quad; optimal cruise power shifted from \approx 200–250 W down to \approx 100–125 W with the wing, without major changes to the multirotor controller [XQa20]. This is a strong, quantitative demonstration that fixed aerodynamic surfaces can more than halve J/m at moderate forward speeds while preserving conventional quad control.

Airfoiled arms Freitas et al. systematically tested airfoiled arms on a quad (DJI F450 class). Arm airfoils reduced arm drag and delivered \sim 19–31% less electrical power in forward flight at 10–15 m/s (depending on angle) and modest improvements to top speed, with negligible hover penalty and no controller change [FDF25]. This is especially attractive for “agility-first” designs where we seek free forward-flight efficiency.

Summary These works collectively show that adding lifting/streamlining surfaces to a quad yields measured cruise efficiency gains (\approx 20–50% power reduction at \approx 10–15 m/s) at minimal implementation cost: no tilting mechanisms, no transitions, and only modest or negligible changes to hover agility if the surfaces are properly sized and decoupled from rotor flows. Importantly, the canonical quadrotor controller stack (geometric/differential-flatness + INDI inner loop) remains applicable, maintaining excellent tracking (\sim few-cm RMS) and high gust robustness documented for agile quads [TK18; FKa22; Sun+21].

3.4 Shrouds and Ducts as Augmentation

Shrouding improves hover power loading and can protect the rotors. MDPI Drones studies report \sim 15–28% improvements in lift and “FM efficiency” for optimized ducted multi-propeller configurations in hover [Li+21]. Classic MAV shroud experiments show up to \sim 30% power-loading gains at small scales [HBC14], and broader surveys note up to $>$ 50% thrust gains or equivalent power reductions in hover for well-designed ducts, but performance degrades at higher advance ratios (forward flight) due to inlet losses and added frontal area [Ca21; Per08]. Thus, shrouds are advantageous for hover/low-speed efficiency and safety but can hurt high-speed efficiency and cross-wind agility—less aligned with our “agile forward-flight efficiency” goal.

3.5 Quantitative Comparison Across Criteria

From the studies above:

Agility Pure multirotors: $\geq 3 g$, $\leq 0.1 \text{ m RMS}$ tracking demonstrated [TK18; FKa22]. Tailsitters: agile aerobatics and 2–3 g transitions are feasible [LGa22; TK22], but hover control surfaces may be saturation-limited in gusts. Quadplanes/tilt designs: agility is generally lower in hover due to added inertia and interference; transitions add constraints [OŁ22; MJa22].

Efficiency (forward flight) Fixed wings/airfoils on quads reduce cruise power by ~20–50% at 10–15 m/s [DD18; XQa20; FDF25]. Shrouds: +15–30% hover power loading, but often worse at higher advance ratios [Li+21; HBC14; Ca21]. Hybrids (tilt/quad-plane/tailsitter) achieve fixed-wing-like J/m at cruise but pay complexity/weight penalties.

Controllability & transitions Multirotors and “quad + wings” avoid mode transitions entirely—hover/forward authority comes from the same actuators; differential-flatness/geometric + INDI covers both regimes [LLM10; TK18]. Hybrids require transition path planning and mode-dependent control allocation [Da24; MJa22].

Robustness to aero disturbances INDI-based quads show strong disturbance rejection without precise aero models [SCM10; SCC17; Sun+21]. Hybrids can be robust, but robustness proofs and quantitative gust testing during transition remain sparse.

Implementation complexity Adding fixed surfaces is mechanically trivial and controller-agnostic; shrouds add structure and possible crosswind penalties; hybrids add mechanisms, sensors, and software complexity (e.g., NMPC with switching and detailed aerodynamics).

3.6 Gaps and Open Issues

Despite progress, three gaps remain:

1. There are few quantitative studies of fixed wings on quads that explicitly preserve aggressive maneuverability ($\geq 3 g$, meter-scale turns) while reporting cruise Wh/km (or J/m) and closed-loop tracking error; most report % power savings at one speed [DD18; XQa20].

2. Disturbance modeling for augmented quads is incomplete, particularly interactions between rotor wakes and wings across the speed envelope and in crosswinds; robust INDI masks some deficiencies, but better disturbance observers/models would inform design trade-offs [Sun+21].
3. For hybrid VTOLs, coordinated-turn performance (load factors, radius, sideslip limits) with full transition dynamics is under-reported; Daud Filho et al. detail transitions but not coordinated turns with quantitative lateral-acceleration margins [Da24].

These gaps motivate a design that seeks measured efficiency gains with minimal impact on agility and low complexity.

3.7 Why a Quadrotor with Fixed Aerodynamic Surfaces?

The literature supports a clear argument:

1. **Preserve hover agility and controllability:** no transitions, mature differential-flatness/geometric + INDI stack with proven centimeter-level tracking and multi-g maneuvers [LLM10; TK18; FKa22].
2. **Capture meaningful cruise-efficiency gains:** $\sim 20\text{--}50\%$ power reduction around 10–15 m/s using wings or airfoilized arms [DD18; XQa20; FDF25], directly lowering J/m and extending range/mission time without complex mechanisms.
3. **Maintain robustness to disturbances via INDI** without high-fidelity aero models [SCM10; SCC17; Sun+21].
4. **Keep implementation complexity low:** fixed surfaces; unchanged propulsion and control allocation, avoiding the mass, moving parts, and software overhead of tilt/transition systems [MJa22; OŁ22].

Given the target criteria—agility, efficiency at cruise, controllability across the envelope, gust robustness, and modest complexity—the evidence favors a quadrotor with fixed aerodynamic surfaces over more complex hybrids.

4 Dynamics Model

This chapter introduces the six-degree-of-freedom (6-DoF) rigid-body model used to describe the motion of the X-wing quadrotor platform. The formulation captures the essential translational and rotational dynamics with lumped aerodynamic effects from the integrated wing surfaces. The model is intended to provide a physically consistent basis for later control design and parameter identification.

4.1 Coordinate Frames and States

The equations of motion are expressed in the world (inertial) and body-fixed frames.

- The **world frame** follows the ENU convention, with gravity $\mathbf{g} = [0, 0, -g]^\top$.
- The **body frame** is located at the vehicle's center of gravity (CoG), with the x -axis pointing forward, y -axis to the left, and z -axis upward, normal to the rotor plane.

The system states are

$$(\mathbf{p}, \mathbf{v}, R, \boldsymbol{\omega}) \in \mathbb{R}^3 \times \mathbb{R}^3 \times SO(3) \times \mathbb{R}^3, \quad (4.1)$$

where \mathbf{p} and \mathbf{v} denote position and linear velocity in the world frame, $R \in SO(3)$ is the rotation matrix from body to world frame, and $\boldsymbol{\omega}$ is the body angular velocity. The control inputs are the individual rotor thrusts

$$\mathbf{u} = [f_1, f_2, f_3, f_4]^\top, \quad (4.2)$$

each acting approximately along the body $+z$ direction. Explicit control allocation and motor dynamics are treated in Chapter 6.

4.2 Forces

The total force acting on the vehicle in the world frame is the sum of gravity, rotor thrust, and aerodynamic forces:

$$\mathbf{F} = m\mathbf{g} + \mathbf{F}_T + R \mathbf{F}_{\text{aero}}. \quad (4.3)$$

4.2.1 Gravity

The gravitational force is given by $m\mathbf{g}$ with m the total mass of the system.

4.2.2 Rotor Thrust

Each rotor i produces a thrust f_i approximately aligned with the body $+z$ axis. The total thrust in the world frame is

$$\mathbf{F}_T = \left(\sum_{i=1}^4 f_i \right) R \mathbf{e}_3. \quad (4.4)$$

4.2.3 Aerodynamic Forces

The fixed aerodynamic surfaces generate lift and drag forces that depend on the body-frame airspeed

$$\mathbf{v}_a = R^\top (\mathbf{v} - \mathbf{v}_w), \quad (4.5)$$

where \mathbf{v}_w is the wind velocity in the world frame. For design and performance estimation, the aerodynamic forces are computed using standard expressions:

$$L = \frac{1}{2}\rho S C_L(\alpha) \|\mathbf{v}_a\|^2, \quad D = \frac{1}{2}\rho S C_D(\alpha) \|\mathbf{v}_a\|^2, \quad (4.6)$$

where ρ is air density, S is the total wing area, and $C_L(\alpha)$ and $C_D(\alpha)$ are the lift and drag coefficients as functions of angle of attack α . We use the approximations $C_L = a_\alpha \alpha$ and $C_D = C_{D0} + kC_L^2$ to estimate the wing contributions during the platform design phase.

However, these aerodynamic forces are **not explicitly modeled in the controller**. Instead, they are treated as external disturbances that are automatically rejected by the incremental nonlinear dynamic inversion (INDI) controller presented in Chapter 6. This approach avoids the need for precise aerodynamic parameter identification or online angle-of-attack estimation, relying on the controller's inherent robustness to unmodeled dynamics.

4.3 Moments

The moments acting on the vehicle are composed of rotor-generated torques and lumped aerodynamic moments:

$$\boldsymbol{\tau} = \boldsymbol{\tau}_T + \boldsymbol{\tau}_{\text{aero}}. \quad (4.7)$$

The rotor moments τ_T arise from thrust lever arms and counter-torques of the propellers, while τ_{aero} accounts for small contributions from the aerodynamic center offset and asymmetric lift distribution. The detailed mapping from individual rotor thrusts to force and moments (control allocation) is treated in Chapter 6.

4.4 Equations of Motion

The rigid-body dynamics of the vehicle are expressed as

$$\dot{\mathbf{p}} = \mathbf{v}, \quad (4.8)$$

$$\dot{\mathbf{v}} = \frac{1}{m} (m\mathbf{g} + \mathbf{F}_T + R\mathbf{F}_{\text{aero}}), \quad (4.9)$$

$$\dot{\mathbf{R}} = R[\boldsymbol{\omega}]_{\times}, \quad (4.10)$$

$$J\dot{\boldsymbol{\omega}} = -\boldsymbol{\omega} \times J\boldsymbol{\omega} + \boldsymbol{\tau}, \quad (4.11)$$

where J is the inertia matrix expressed in the body frame, and $[\boldsymbol{\omega}]_{\times}$ denotes the skew-symmetric matrix representation of the cross product.

4.5 Assumptions and Simplifications

The following assumptions are made to keep the model tractable:

- Quasi-steady aerodynamics; unsteady and dynamic-stall effects are neglected.
- No prop-wash coupling or aerodynamic interference between rotors and wings.
- Symmetric mass and inertia distribution with negligible structural flexibility.
- Fixed-pitch rotors; gyroscopic and blade flapping effects are ignored.
- Aerodynamic forces and moments are treated as lumped, quasi-linear disturbances for identification.

4.6 Remarks

The presented model provides a concise yet comprehensive description of the platform's motion. It captures the key couplings between thrust, gravity, and aerodynamic effects while remaining simple enough for real-time simulation and control. In later chapters, this model forms the foundation for the geometric and incremental nonlinear dynamic inversion (INDI) control strategies, which compensate for the unmodeled aerodynamic disturbances in flight.

5 Platform Design

5.1 Platform Design

We design an aerodynamic surface-enhanced quadrotor in an X-wing configuration to preserve the agility of a conventional multirotor while benefiting from passive lift in forward flight. The design objective was to create a platform that remains fully compatible with existing quadrotor control architectures while achieving improved aerodynamic efficiency in the moderate-speed regime of 5 m s^{-1} to 15 m s^{-1} . This range was chosen to match the operational envelope of modern visual-inertial odometry and path-planning algorithms, which rely on sufficient feature persistence and computation time when traversing complex environments. The platform maintains full hover capability and allows seamless transition between flight regimes, including the ability to come to a complete stop in the case of unexpected obstacles or path-planning delays.

5.1.1 Configuration and Layout

The overall configuration follows a conventional X-shaped quadrotor layout in which each rotor arm is extended into a fixed aerodynamic lifting surface, forming an “X-wing” planform. This choice leverages the inherent structural arrangement of a quadrotor—four arms symmetrically distributed around the center of gravity—while enabling these arms to generate lift instead of purely supporting the motors. Alternative configurations such as a “plus” (+) layout or biplane arrangements were considered less favorable: in a + configuration, two wings would be vertically oriented and thus unable to generate lift, while a biplane would require additional structural connections between the upper and lower planes, adding mass and complexity. The X-wing approach allows a single compact central frame with minimal added mass.

Each of the four wings has a span of 0.45 m and a chord of 0.25 m, resulting in an aspect ratio of approximately 1.8. The wing span was chosen to accommodate readily available 0.5 m carbon rods used as internal spars, simplifying construction while placing the platform in the target cruise speed range of approximately 10 m s^{-1} , where full aerodynamic lift would support the vehicle weight. The chord length was constrained by the available 3D printer build volume of just over 250 mm; longer chords would have exceeded printability limits. The motor mounting legs, which

position the motors in front of the wings and provide landing feet to avoid landing directly on the wing trailing edges, were printed diagonally within the build volume, further informing the final chord dimension. This value provides a balance between aerodynamic efficiency and structural stiffness; higher aspect ratios would improve lift–drag performance but increase bending inertia and reduce agility. The total diagonal motor-to-motor distance is 1.1 m. All wings are mounted with alternating dihedral and anhedral angles of $\pm 45^\circ$, creating a fully symmetric configuration independent of flight direction. This symmetry enables the same controller gains to be used in roll and pitch and allows the yaw heading to be freely adjusted depending on which orientation minimizes control effort.

The wings are untwisted and employ a NACA 0015 symmetric airfoil. The choice of a symmetric section was motivated by the requirement for bidirectional flight and simple aerodynamic modeling. The thickness ratio of 15% conveniently accommodates the two internal carbon spars used for stiffness and assembly. The NACA 0015 profile also exhibits a delayed stall and smooth lift curve, beneficial during transition and moderate-angle flight conditions. The chord line of each wing is aligned with the average rotor thrust axis (noting that the motors are tilted $\pm 5^\circ$ for yaw authority, as discussed below), such that the average motor thrust is directed vertically downward in hover without inducing horizontal force components. This alignment prioritizes hover efficiency, though tilting the wings relative to the motor thrust could improve forward-flight performance by allowing the motors to contribute a greater vertical component while the wings operate at reduced angles of attack.

The wings are printed from PLA Aero filament and contribute a total of approximately 440 g to the vehicle mass. All non-propulsive components (flight controller, companion computer, and batteries) are mounted near the geometric center, at $x = y = 0$, distributed symmetrically about the $z = 0$ plane to ensure balanced inertia. The complete airframe, including center hub and motor mounts, is fully 3D-printed. No structural asymmetries or significant vibrations were observed during geometric control experiments. However, when using the INDI controller, elastic wing vibrations appeared in the IMU data. To mitigate this, thin lines were tensioned between neighboring wings to increase stiffness and shift the dominant resonance frequency upward, improving signal filtering and control stability.

5.1.2 Wing Aerodynamics

The aerodynamic surfaces were designed for efficient lift generation in the cruise speed range of 5 m s^{-1} to 15 m s^{-1} . At a nominal flight velocity of 10 m s^{-1} and chord length of 0.25 m, the expected Reynolds number is on the order of 1×10^5 – 2×10^5 , placing the operation in the low-Reynolds transitional regime.

The Reynolds number characterizes the ratio of inertial to viscous forces and is computed as

$$Re = \frac{\rho V c}{\mu} = \frac{V c}{\nu}, \quad (5.1)$$

where ρ is the air density, V is the airspeed, c is the chord length, μ is the dynamic viscosity, and ν is the kinematic viscosity of air. Using standard atmospheric conditions at sea level ($\rho = 1.225 \text{ kg/m}^3$, $\nu = 1.4207 \times 10^{-5} \text{ m}^2/\text{s}$) and the wing chord length of $c = 0.25 \text{ m}$, Table 5.1 shows the Reynolds numbers across the operational flight envelope.

Table 5.1: Reynolds numbers for the NACA 0015 wing at various airspeeds with chord length $c = 0.25 \text{ m}$ at sea-level conditions.

Airspeed [m s ⁻¹]	Reynolds Number [-]
5	87,900
10	175,800
15	263,700
20	351,600
25	439,500
30	527,400

At these conditions, the NACA 0015 profile provides a lift coefficient slightly below unity ($C_L \approx 0.9$) and a drag coefficient of approximately $C_D = 0.08$. The target angle of attack in steady cruise was set to around 10° . Figure 5.1 shows the predicted lift coefficient for the NACA 0015 airfoil at two Reynolds numbers representative of the operating regime, computed using XFLR5 with NCrit=5 to account for free-stream turbulence typical of outdoor flight. At the design cruise angle of attack ($\alpha \approx 10^\circ$), the airfoil achieves $C_L \approx 0.9\text{--}1.0$, providing sufficient lift to support the vehicle weight at moderate forward speeds.

Lift and drag forces were estimated using the analytical model introduced earlier,

$$L = \frac{1}{2}\rho S C_L(\alpha) \|v_a\|^2, \quad D = \frac{1}{2}\rho S C_D(\alpha) \|v_a\|^2,$$

with ρ denoting air density, S the total projected wing area, and v_a the airspeed relative to the body. These analytical estimates guided the sizing of the vehicle and the placement of the aerodynamic surfaces relative to the center of gravity.

Quantitative estimate at 12 m/s. Using $\rho = 1.225 \text{ kg/m}^3$, total projected wing area $S \approx 0.318 \text{ m}^2$, $C_L \approx 0.9$ at $\alpha \approx 10^\circ$, and $C_D \approx 0.18$, we obtain

$$L = \frac{1}{2}\rho S C_L V^2 \approx \frac{1}{2} \cdot 1.225 \cdot 0.318 \cdot 0.9 \cdot (12)^2 \approx 25.25 \text{ N},$$

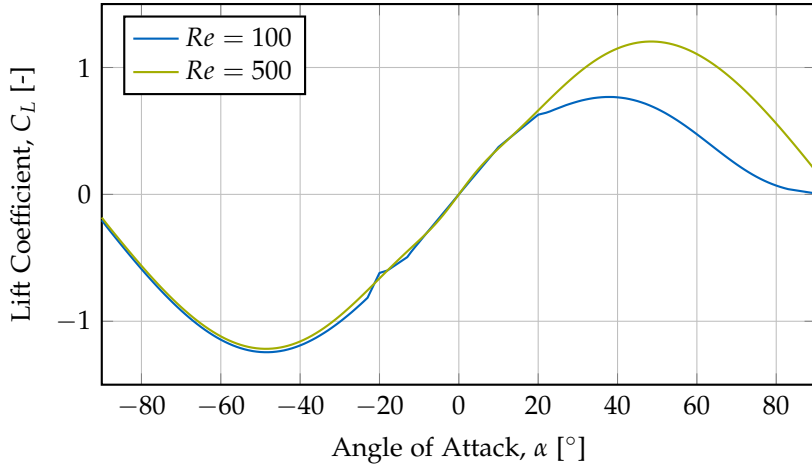


Figure 5.1: Lift coefficient for the NACA 0015 airfoil at two Reynolds numbers as a function of angle of attack, computed using XFLR5 with NCrit=5. The design cruise angle of attack of approximately 10° provides $C_L \approx 0.9\text{--}1.0$ across the operating Reynolds number range.

$$D = \frac{1}{2} \rho S C_D V^2 \approx \frac{1}{2} \cdot 1.225 \cdot 0.318 \cdot 0.18 \cdot (12)^2 \approx 5.05 \text{ N.}$$

For the 2.5 kg platform ($W \approx 24.53$ N), the wings supply $\approx 103\%$ of the weight at 12 m/s, meaning the rotors can reduce thrust significantly and primarily need to overcome aerodynamic drag and provide control authority. The wing-induced drag corresponds to ≈ 60.6 W of propulsive power at 12 m/s ($P_D = DV$), not accounting for additional parasite/induced drag from the fuselage, rotors, and interference effects. These values are first-order estimates in the low- Re regime and neglect propeller-wing interaction; they nonetheless quantify the expected forward-flight relief on rotor-induced power.

Propeller-wing interaction effects were not explicitly studied in this work. Since the wings are aligned with the rotor arms, partial overlap between the propeller wake and wing surface occurs, but its contribution to performance is assumed to be secondary compared to the main aerodynamic lift of the forward wings. Future investigations could employ CFD or wind-tunnel testing to quantify this coupling.

5.1.3 Propulsion and Actuation

The propulsion system was designed to maintain high agility while achieving efficient cruise performance. A thrust-to-weight ratio exceeding 3 was selected as a design target, enabling the vehicle to perform aggressive maneuvers and sustain up to 3 g

lateral acceleration, consistent with agility metrics reported in the multirotor literature. To meet this target, high-response racing-grade components were chosen: T-MOTOR VELOX V2808 motors combined with HQProp $7 \times 3.5 \times 3$ three-blade propellers. The resulting hover throttle is approximately 30%, leaving sufficient control margin for disturbance rejection and attitude stabilization.

Motor and propeller performance were characterized experimentally to obtain both thrust and torque mappings. The measurements were performed using a single motor mounted on a six-axis force–torque sensor, with forces and torques recorded over a range of command inputs. The empirical relations between motor command, thrust, and torque were used to map the controller outputs into corresponding DShot commands for the flight controller. These mappings also served to estimate instantaneous energy consumption and mechanical efficiency during flight trials.

The motors are tilted outward by 5° to increase effective yaw torque authority. In the control model, this tilt is represented as a small rotation of the individual thrust vectors, effectively increasing the available moment around the vertical axis. No DShot timing modifications were required, and no direct RPM feedback control was implemented. Instead, the INDI controller integrates motor speed responses and compensates for small deviations, ensuring smooth dynamic performance.

Although the addition of wings increases the total inertia of the platform, particularly in yaw, the resulting damping improved stability and reduced sensitivity to high-frequency disturbances. No significant cross-coupling between roll and pitch dynamics was observed. Overall, the X-wing configuration provides a good compromise between efficiency and agility, maintaining the control simplicity of a quadrotor while offering measurable lift benefits in forward flight. Performance gains were compared analytically against a non-winged reference quadrotor of comparable size and propulsion, confirming a theoretical reduction in power consumption at moderate forward velocities.

6 Control Architecture

This chapter presents the flight control system used on the X-wing quadrotor. The architecture combines (i) *flatness-based reference generation* for dynamically feasible trajectories, (ii) a *geometric outer loop* on $SE(3)$ that turns translational tracking errors into desired attitude and collective thrust, and (iii) an *Incremental Nonlinear Dynamic Inversion (INDI)* inner loop that realizes the requested angular dynamics while rejecting unmodeled aerodynamic effects from the wings. The wings are *not* explicitly modeled in the controller; instead, their influence is treated as a disturbance and compensated incrementally by INDI [SCC16; Oos+17; Kam+18; Tzo+21].

6.1 Reference Generation

Quadrotor dynamics are differentially flat with respect to $\mathbf{p}_d = [x_d, y_d, z_d]^\top$ and ψ_d . We generate $(\mathbf{p}_d, \dot{\mathbf{p}}_d, \ddot{\mathbf{p}}_d, \psi_d)$ from a minimum-snap polynomial or flatness-based planner; jerk/snap may be used internally for smoothness but are not required by the controller interface.

Coordinated-turn option. In forward flight, sideslip can be bounded by aligning the body x -axis with the horizontal velocity and setting a yaw-rate reference approximately as

$$\dot{\psi}_d \approx \frac{a_{y,d}}{V_d \cos \theta_d}, \quad (6.1)$$

where $a_{y,d}$ is the desired lateral acceleration, $V_d = \|\dot{\mathbf{p}}_d\|$, and θ_d the pitch. We use this option when tracking fast, curving trajectories; otherwise ψ_d follows a commanded heading.

6.2 Geometric Outer Loop

The outer loop maps position/velocity errors to a desired attitude $R_d \in SO(3)$ and a collective thrust f_{coll} .

6.2.1 Translational feedback and force target

Let $\tilde{\mathbf{p}} = \mathbf{p}_d - \mathbf{p}$ and $\tilde{\mathbf{v}} = \dot{\mathbf{p}}_d - \mathbf{v}$. With diagonal gains $\mathbf{k}_p, \mathbf{k}_v > 0$ (elementwise),

$$\mathbf{a}_c = \mathbf{k}_p \odot \tilde{\mathbf{p}} + \mathbf{k}_v \odot \tilde{\mathbf{v}} + \ddot{\mathbf{p}}_d - \mathbf{g}, \quad (6.2)$$

defines the nominal commanded acceleration in the world frame (ENU, $\mathbf{g} = [0, 0, -g]^\top$).

Aerodynamic feedforward from onboard sensing. We estimate a body-frame specific force \mathbf{a}_B from the IMU (bias-compensated) or a model fallback and low-pass filter it, $\mathbf{a}_{B,f} = \text{LPF}_a(\mathbf{a}_B)$. From filtered motor speeds ω_m we form $\mathbf{f}_f = k_t \text{LPF}_m(\omega_m^{\circ 2}) + \mathbf{b}$, so that $f_{T,f} = \mathbf{1}^\top \mathbf{f}_f$. A world-frame aero-compensation term follows as

$$\mathbf{a}_{\text{aero}} = R \left(\frac{f_{T,f}}{m} \mathbf{e}_3 - \mathbf{a}_{B,f} \right), \quad \mathbf{a}_c \leftarrow \mathbf{a}_c + \mathbf{a}_{\text{aero}} \text{ if } z > 0.5 \text{ m.} \quad (6.3)$$

Intuitively, $R(f_{T,f}\mathbf{e}_3/m)$ is the thrust-induced specific force in the world; subtracting the measured specific force yields the unmodeled aero contribution to be fed forward.

6.2.2 Attitude target and thrust projection

We set the desired body z -axis to the direction of the commanded acceleration, $\mathbf{z}_B^d = \mathbf{a}_c / \|\mathbf{a}_c\|$. For heading, we prefer a coordinated-turn alignment:

$$\mathbf{x}_c = \begin{cases} \dot{\mathbf{p}}_d / \|\dot{\mathbf{p}}_d\|, & \|\dot{\mathbf{p}}_d\| > 0.2 \text{ m/s,} \\ R_z(\psi_d) \mathbf{e}_x, & \text{otherwise,} \end{cases} \quad (\mathbf{x}_c)_z = 0, \quad \|\mathbf{x}_c\| = 1.$$

To avoid the degeneracy $\mathbf{z}_B^d \parallel \mathbf{x}_c$, we set $\mathbf{x}_c \leftarrow -\mathbf{e}_z$ if $\angle(\mathbf{z}_B^d, \mathbf{x}_c) < 5^\circ$. Then

$$\mathbf{y}_B^d = \frac{\mathbf{z}_B^d \times \mathbf{x}_c}{\|\mathbf{z}_B^d \times \mathbf{x}_c\|}, \quad \text{flip } \mathbf{y}_B^d \text{ if } (\mathbf{y}_B^d)^\top (R \mathbf{e}_y) < 0, \quad \mathbf{x}_B^d = \frac{\mathbf{y}_B^d \times \mathbf{z}_B^d}{\|\mathbf{y}_B^d \times \mathbf{z}_B^d\|}, \quad (6.4)$$

and $R_d = [\mathbf{x}_B^d \ \mathbf{y}_B^d \ \mathbf{z}_B^d]$. We compute collective thrust by projection to reduce transients:

$$f_{\text{coll}} = m \mathbf{a}_c^\top (R \mathbf{e}_3). \quad (6.5)$$

6.2.3 Tilt-prioritized attitude control and rate reference

Following the tilt-prioritized design of Föhn (2020), with attitude error $q_e = q^{-1} \otimes q_d$ and gains $k_{\text{att},xy}, k_{\text{att},z}$,

$$T_{\text{att}} = \text{diag}(k_{\text{att},xy}, k_{\text{att},xy}, k_{\text{att},z}), \quad (6.6)$$

$$\mathbf{t}(q_e) = \begin{bmatrix} q_{e,w}q_{e,x} - q_{e,y}q_{e,z} \\ q_{e,w}q_{e,y} + q_{e,x}q_{e,z} \\ q_{e,z} \end{bmatrix}, \quad \text{if } q_{e,w} \leq 0 \text{ then } t_3 \leftarrow -t_3, \quad (6.7)$$

$$\boldsymbol{\omega}_d = \frac{2}{\sqrt{q_{e,w}^2 + q_{e,z}^2}} T_{\text{att}} \mathbf{t}(q_e). \quad (6.8)$$

A simple rate-plus-error form produces an *angular-acceleration proxy* for INDI:

$$\boldsymbol{\alpha}_d = \boldsymbol{\omega}_d + \mathbf{k}_{\text{rate}} \odot (\boldsymbol{\omega}_d - \boldsymbol{\omega}). \quad (6.9)$$

We forward $(R_d, f_{\text{coll}}, \boldsymbol{\alpha}_d)$ to the inner loop.

6.3 INDI Inner Loop

The inner loop realizes the requested rotational dynamics robustly without an explicit aerodynamic model. Over a small sampling interval Δt , the change in the measured output \mathbf{y} (specific force or angular acceleration proxy) satisfies

$$\Delta \mathbf{y} \approx B \Delta \mathbf{u}, \quad (6.10)$$

with B the (local) control-effectiveness matrix and $\Delta \mathbf{d}$ (disturbance change) second order in Δt ; hence the incremental update largely cancels unmodeled aerodynamics [SCC16; Oos+17; Kam+18; Tzo+21].

6.3.1 Measured/filtered quantities

We use gyroscope rates $\boldsymbol{\omega}$ and their filtered derivative as an acceleration proxy,

$$\dot{\boldsymbol{\omega}}_f = \frac{d}{dt} (\text{LPF}_{\boldsymbol{\omega}}(\boldsymbol{\omega})), \quad (6.11)$$

and reconstruct filtered rotor thrusts from motor speeds as in (6.3). The filtered rotor moments follow from the allocation matrix G :

$$\begin{bmatrix} f_{T,f} \\ \boldsymbol{\tau}_f \end{bmatrix} = G \mathbf{f}_f. \quad (6.12)$$

6.3.2 Nominal NDI versus incremental INDI moments

Let $\boldsymbol{\mu} = [\mu_0, \mu_x, \mu_y, \mu_z]^\top = [f_T, \tau_x, \tau_y, \tau_z]^\top$. We form two moment requests:

$$\boldsymbol{\mu}_{\text{NDI}} = \begin{bmatrix} m f_{\text{coll}} \\ (J\boldsymbol{\alpha}_d + \boldsymbol{\omega} \times J\boldsymbol{\omega})_x \\ (J\boldsymbol{\alpha}_d + \boldsymbol{\omega} \times J\boldsymbol{\omega})_y \\ (J\boldsymbol{\alpha}_d + \boldsymbol{\omega} \times J\boldsymbol{\omega})_z \end{bmatrix}, \quad (6.13)$$

$$\boldsymbol{\mu}_{\text{INDI}} = \begin{bmatrix} m f_{\text{coll}} \\ \boldsymbol{\tau}_f + J(\boldsymbol{\alpha}_d - \dot{\boldsymbol{\omega}}_f) \end{bmatrix}. \quad (6.14)$$

Equation (6.14) is the incremental update: the moment change uses the mismatch between desired and measured angular accelerations, injecting the *measured* effectiveness J and $\boldsymbol{\tau}_f$.

Yaw-stability tweak. To avoid yaw oscillations observed in practice, we blend the two requests and set

$$\mu_z \leftarrow (\boldsymbol{\mu}_{\text{NDI}})_z, \quad (6.15)$$

while keeping roll/pitch from (6.14).

Mode switch at low altitude. For takeoff and near-ground operation we disable INDI and use $\boldsymbol{\mu} \leftarrow \boldsymbol{\mu}_{\text{NDI}}$ if $z < 0.5$ m or a configuration flag is off.

6.3.3 Update to rotor thrusts

With the inverse allocation matrix G^{-1} (precomputed from geometry, including motor tilt), the commanded rotor thrusts are

$$\mathbf{u} = G^{-1} \boldsymbol{\mu}, \quad f_T = \mathbf{1}^\top \mathbf{u}. \quad (6.16)$$

Each rotor thrust maps to speed via the quadratic thrust curve,

$$f_i = k_t \omega_i^2 + b_i, \quad \omega_i = \sqrt{\max(0, (f_i - b_i)/k_t)}. \quad (6.17)$$

Commands are sent to the ESCs (DShot). Saturation and safety guards are applied at the actuation layer.

6.4 Control Allocation and Constraints

The allocation matrix $G \in \mathbb{R}^{4 \times 4}$ maps individual rotor thrusts to total thrust and body moments,

$$\boldsymbol{\mu} = G \mathbf{u}, \quad \mathbf{u} = [f_1, f_2, f_3, f_4]^\top, \quad (6.18)$$

and encodes the arm geometry and 5° motor tilt (see Chapter 7). We use its inverse for real-time mapping (6.16). Commanded thrusts are clipped to $f_i \in [f_{\min}, f_{\max}]$ and total thrust is bounded for hardware safety. (When needed, a constrained least-squares allocator can replace G^{-1} to enforce non-negativity and torque bounds.)

6.5 Implementation Notes

Filtering. First-order low-pass filters $\text{LPF}_a, \text{LPF}_\omega, \text{LPF}_m$ use cutoffs chosen below the control bandwidth to avoid amplifying sensor noise in $\dot{\omega}_f$. All filters are tuned consistently across the outer/inner loops.

Sensing and fusion. The controller runs with IMU rates at high frequency; position/velocity references come from Vicon or onboard state estimation. Delays are kept small by using incremental updates; no explicit delay compensation was required.

Scheduling. The inner INDI loop runs faster than the outer geometric loop (rate separation). Allocation and motor mapping execute at the inner-loop rate.

Logging and health. We log $\omega, \dot{\omega}_f, \mathbf{f}_f, \tau_f$ and the residual $\tau_f - J\dot{\omega}_f - \omega \times J\omega$ to monitor effectiveness. Guard checks reject invalid states or setpoints.

6.6 Tuning Guidance

- **Outer loop $\mathbf{k}_p, \mathbf{k}_v$:** increase until overshoot appears in step tests, then back off; clip $\tilde{\mathbf{p}}, \tilde{\mathbf{v}}$ to limit transients.
- **Attitude gains $k_{\text{att},xy}, k_{\text{att},z}$:** prioritize $x-y$ for agility; keep $k_{\text{att},z}$ smaller to avoid yaw chatter.
- **Rate gains \mathbf{k}_{rate} :** start small; raise until $\dot{\omega}_f$ tracks α_d with minimal lag.
- **Filters:** set cutoffs so that $\dot{\omega}_f$ is smooth but responsive; align motor-speed and accelerometer filter cutoffs.

- **Allocation:** verify G from CAD (arm length, tilt, motor spin) and validate G^{-1} via static torque tests.

6.7 Summary

The proposed control system stacks a geometric $SE(3)$ outer loop with an INDI inner loop. The outer loop produces $(R_d, f_{\text{coll}}, \alpha_d)$ by combining proportional-derivative translational feedback with an aero feedforward term from onboard sensing, and a coordinated-turn attitude construction. The INDI layer then incrementally inverts the rotational dynamics using measured effectiveness, blending a nominal NDI yaw to suppress oscillations. This architecture achieves robust tracking across hover and forward-flight regimes while compensating for the unmodeled aerodynamic influence of the X-wing surfaces.

7 Experimental Setup

7.1 Experimental Setup

This section documents the hardware configuration, software stack, and test facilities that enabled the experimental evaluation of the aerodynamic surface-enhanced quadrotor. The setup was designed to be fully reproducible, with all control and estimation software running on open frameworks and all data recorded for subsequent analysis.

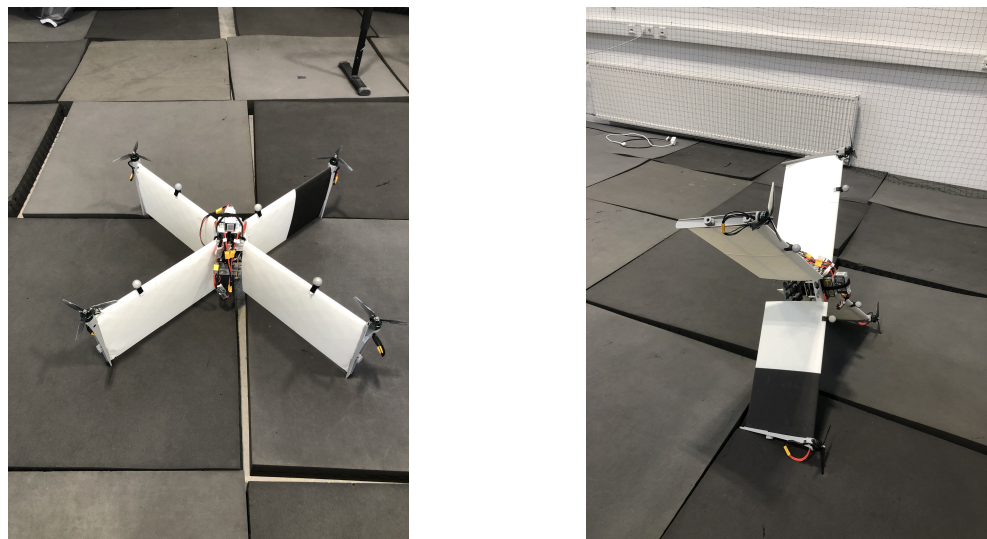
7.1.1 Hardware

Airframe and Propulsion

The experimental platform consists of an X-wing aerodynamic surface-enhanced quadrotor (Fig. 7.1) with a total mass of 2.5 kg (without batteries: 1.75 kg). Each of the four T-MOTOR VELOX V2808 motors produces a maximum static thrust of approximately 22 N, resulting in a total available thrust of 88 N and a thrust-to-weight ratio of 3.59 at nominal 22.2 V (6S LiPo). The propulsion system employs HQProp 7×3.5×3 three-blade racing propellers optimized for medium–high efficiency in the forward-flight regime.

The wings feature a NACA 0015 airfoil with a span of 450 mm and a chord of 250 mm. Four identical fixed wings are arranged orthogonally (90° between adjacent wings) and mounted with alternating dihedral and anhedral angles of $\pm 45^\circ$. The wings are attached to the central frame using two carbon spars (10 mm outer diameter) clamped into the core structure, allowing for fast removal. The center frame and motor mounts are 3D-printed from standard PLA, while the wing surfaces are printed from lightweight PLA Aero. The total projected horizontal area of all wings is approximately $S_t = 0.318 \text{ m}^2$.

Each motor is mounted with a 5° tilt to improve yaw authority. The center of gravity is located at the geometric center of the vehicle, aligned with the midpoint between all four motors, and approximately at one quarter of the wing chord length from the leading edge.



(a) Top view showing X-wing configuration with orthogonal wing arrangement.

(b) Side view showing alternating dihedral/anhedral wing angles.

Figure 7.1: The experimental X-wing aerodynamic surface-enhanced quadrotor platform.

Thrust Characterization and Command Mapping

To accurately relate motor command inputs to generated thrust, a static thrust characterization was performed for the chosen motor–propeller configuration. A single T-MOTOR VELOX V2808 motor equipped with an HQProp 7×3.5×3 propeller was mounted on a six-axis force–torque sensor (Rokubi Mini) using a custom 3D-printed fixture. The setup allowed precise measurement of the vertical force while commanding the motor through the same DShot interface used in flight (Fig. 7.2).

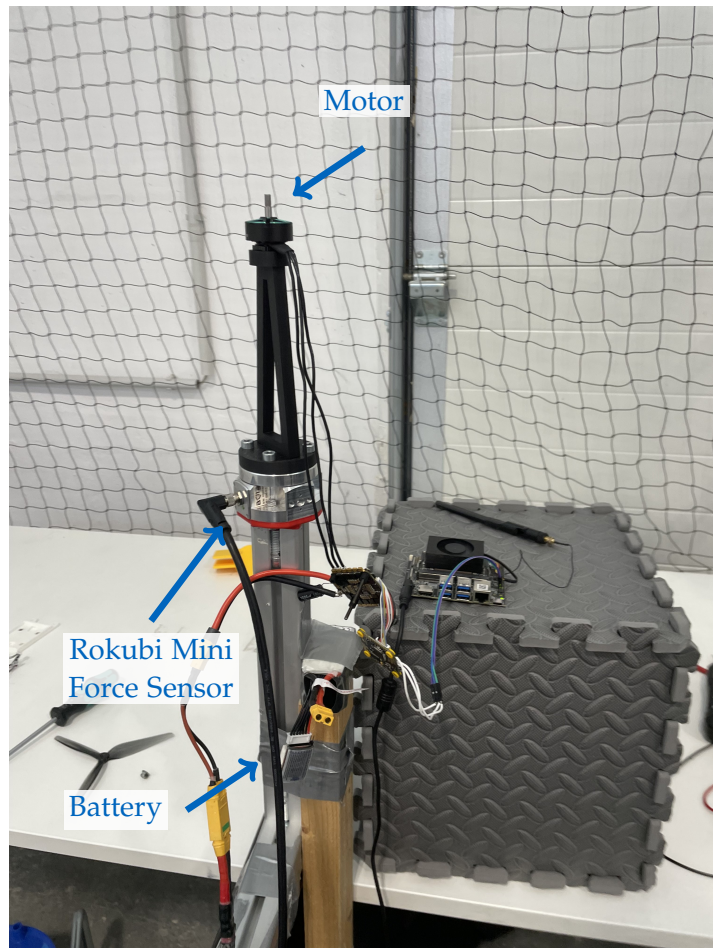


Figure 7.2: Static thrust characterization test stand with motor mounted on Rokubi Mini force–torque sensor.

Motor command values were swept across the full throttle range in incremental steps, and the resulting thrust was recorded. Each command level was averaged over a

2 s window to mitigate transient effects. The measurements yielded a nonlinear but monotonic mapping between normalized command input $u \in [0, 1]$ and thrust output T , which was fitted with a second-order polynomial of the form

$$T(u) = a_2 u^2 + a_1 u + a_0, \quad (7.1)$$

where the coefficients a_i were obtained via least-squares regression.

This empirical mapping was subsequently integrated into the control pipeline to convert desired thrust values from the INDI controller into per-motor DShot commands. The calibrated relationship improved the accuracy of total thrust estimation and allowed for energy-based efficiency analysis during flight tests.

Power configuration considerations. During the bench tests, one motor was mounted on the force sensor while the remaining four motors stayed on the vehicle and were kept fixed. We observed that the command-to-thrust relationship depends on how many motors are simultaneously powered from the battery due to load-dependent voltage sag and internal resistance effects. In particular, running only a single motor from a single 6S pack produced a slightly different mapping than powering all four motors from the flight-representative configuration with two 6S packs in parallel (6S 2P). Unless stated otherwise, the mapping used for control in flight was calibrated under the latter 6S 2P, four-motor-powered condition, and all subsequent thrust conversions refer to this configuration.

Avionics and Electrical System

The avionics stack is based on a *Kakute H7 v1.5* flight controller paired with a 4-in-1 ESC. Two 1400 mA h 6S Tattu R-Line batteries are connected in parallel to power the propulsion and avionics subsystems, resulting in an effective 2800 mA h capacity. The onboard computer, an NVIDIA Jetson Orin Nano (8 GB), is powered independently from a 1800 mA h 4S LiPo battery.

A custom-modified version of *Betaflight* firmware was employed on the flight controller to extract motor RPM and battery voltage data from the DShot interface and stream them over MAVLink. This modification was necessary because the stock Betaflight implementation does not support publishing these telemetry values via MAVLink. The onboard IMU integrated into the Kakute H7 was used for all experiments; no external IMUs were installed. Vicon markers were arranged asymmetrically to ensure unambiguous pose tracking.

Table 7.1: Bill of Materials (BOM) for the experimental platform.

Category	Component	Model / Key Specs
Airframe	Frame	X-wing center frame with carbon wing spars
Airframe	Wings	Four fixed wings (each 450×250 mm; NACA 0015 airfoil), orthogonal layout (90° between adjacent wings); skins: Bambu Lab PLA Aero; spars: 10 mm OD carbon tubes; total projected horizontal area $S_t \approx 0.318 \text{ m}^2$
Propulsion	Motors ($\times 4$)	T-MOTOR VELOX V2808, max 22 N each
Propulsion	Propellers ($\times 4$)	HQProp 7 \times 3.5 \times 3, 3-blade racing propeller (7", light grey)
Avionics	FC+ESC	Kakute H7 v1.5 Stack (4-in-1 ESC)
Power	Battery ($\times 2$, parallel)	Tattu R-Line V5.0 6S 1400 mAh 150C, XT60; effective 6S 2800 mAh (parallel)
Companion	Computer	Jetson Orin Nano 8 GB (Ubuntu 20.04)
Companion	Power	Tattu R-Line V3.0 4S 1800 mAh 120C, XT60
Motion Capture	Markers	Four 2 cm markers arranged in an asymmetric constellation

7.1.2 Software

Architecture and Communication

The onboard software stack consists of *ROS 1 Noetic* running on the Jetson companion. The geometric controller with inner and outer INDI (Incremental Nonlinear Dynamic Inversion) loops was implemented in ROS and executed on the companion, which sent individual motor speed commands directly to the flight controller over MAVLink via UART. The flight controller, in turn, only relayed the received motor commands to the ESCs while providing IMU, motor RPM, and battery telemetry back to the companion.

A ROS master node was hosted on a ground station computer, while the Jetson ran a ROS node for flight control and data logging. Communication between the two systems was established via Wi-Fi. The ground station handled trajectory loading, arming, and manual control interfaces. All experiment data, including position, velocity, attitude, thrust commands, and battery voltage, were logged in *rosbag* format for offline analysis in Python.

Estimation and Control

The state estimation pipeline used the Vicon motion capture system to provide real-time position and attitude feedback to the controller. In some experiments, an onboard

Extended Kalman Filter (EKF) fused IMU data for state estimation. The Vicon system and onboard IMU operated in a consistent right-handed coordinate convention (front-left-up), with roll about the x -axis, pitch about y , and yaw about z .

All flight maneuvers, including point-to-point transitions and trajectory tracking, were executed fully autonomously from predefined setpoints. No separate failsafe was implemented for Vicon loss, but trajectories could be manually stopped and the vehicle landed or disarmed from the base station.

7.1.3 Facilities

Motion Capture Systems

Two different Vicon systems were employed for data acquisition and feedback. The smaller test arena in Munich measured approximately $7\text{ m} \times 8\text{ m}$ and was used primarily for agility experiments, such as 3 g circle maneuvers. The larger *AIDA Hall* at Reutlingen University provided a volume of about $60\text{ m} \times 45\text{ m}$, enabling steady forward-flight efficiency trials (see Fig. 7.3). Both systems operated at a sampling rate of 200 Hz . Vicon data were used both as ground truth and as feedback for the control loop.



Figure 7.3: AIDA Hall test facility used for efficiency trials (image credit: Reutlingen University [Reu24]).

Test Protocols

Agility tests were performed in the Munich indoor arena equipped with safety nets and a soft landing surface. Efficiency tests were conducted in the AIDA Hall under still-air indoor conditions, with no wind sources or obstacles. Energy consumption was estimated from measured voltage, current draw, and propeller rotational speed data. Typical flight durations were approximately five minutes per run.

Documentation

All experiments were recorded through *rosbag* logs and video footage to facilitate data visualization and reproducibility. Post-processing and analysis were conducted in Python, using custom scripts for trajectory evaluation, energy estimation, and control performance comparison.

8 Experiments and Evaluation

We design experiments to validate thrust mapping, agility/controllability, aerodynamic disturbance characterization, and efficiency gains.

8.1 Thrust map identification

Throttle-to-thrust and RPM-to-thrust mapping; present identified curves and fitted models.

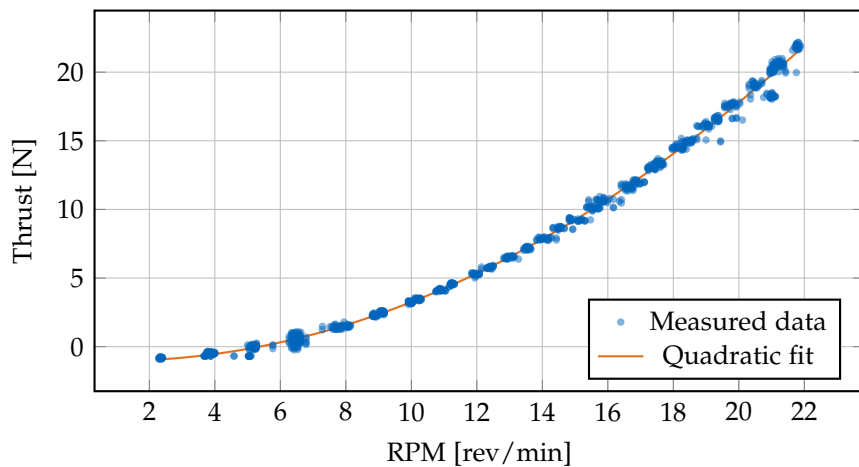


Figure 8.1: Thrust vs RPM with quadratic fit: $T = 0.0515 \cdot \text{RPM}^2 - 0.0902 \cdot \text{RPM} - 0.996$ (N). $R^2 = 0.997$.

8.2 Agility and tracking

- 3g circles in flight arena; metrics: RMS position/altitude tracking error, control effort.

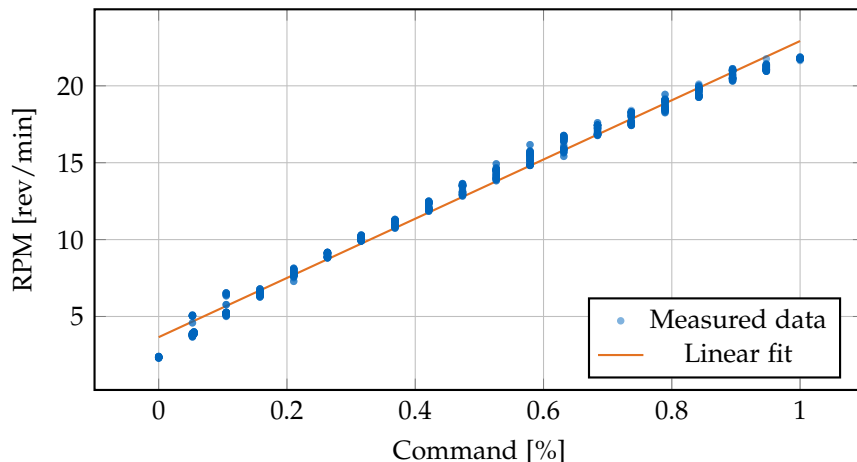


Figure 8.2: RPM vs Command with linear fit: $\text{RPM} = 19.26 \cdot \text{cmd} + 3.65 (rev/min). $R^2 = 0.991$.$

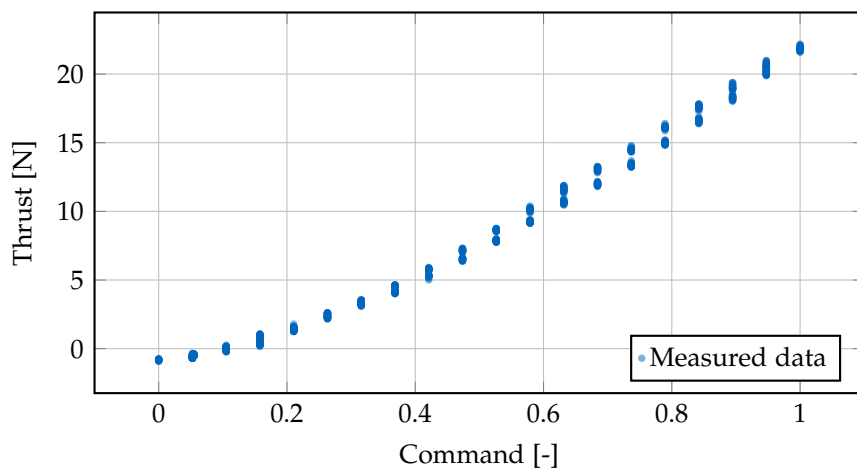


Figure 8.3: Thrust vs Command showing the direct relationship between motor command and thrust force.

8.3 Aerodynamic forces/moment quantification

- Identify equivalent k_D, k_L or $C_L(\alpha), C_D(\alpha)$ from maneuvering flight data; discuss sensitivity.

8.4 Efficiency assessment

- Compare theoretical quad thrust input vs. measured thrust input in AIDA hall flights; quantify energy savings due to passive lift.

8.5 Baseline comparison

- Compare against baseline quadrotor controller without INDI or without wings.

9 Conclusion

We summarize contributions: design of an aerodynamic surface-enhanced quadrotor, a robust INDI-based tracking controller, and experimental validation demonstrating accurate agile tracking and improved forward-flight efficiency. We outline future work, including refined aerodynamic modeling, coordinated-turn guidance integration, and extended outdoor testing.

Abbreviations

- UAV** Unmanned Aerial Vehicle
MAV Micro Air Vehicle
VTOL Vertical Take-Off and Landing
INDI Incremental Nonlinear Dynamic Inversion
EoM Equations of Motion
DoF Degrees of Freedom
CoG Center of Gravity
CoP Center of Pressure
IMU Inertial Measurement Unit
Vicon Vicon Motion Capture System
FC Flight Controller
ESC Electronic Speed Controller
RPM Revolutions per Minute

List of Figures

5.1	Lift coefficient for the NACA 0015 airfoil at two Reynolds numbers as a function of angle of attack, computed using XFLR5 with NCrit=5. The design cruise angle of attack of approximately 10° provides $C_L \approx 0.9\text{--}1.0$ across the operating Reynolds number range.	15
7.1	The experimental X-wing aerodynamic surface-enhanced quadrotor platform.	24
7.2	Static thrust characterization test stand with motor mounted on Rokubi Mini force-torque sensor.	25
7.3	AIDA Hall test facility used for efficiency trials (image credit: Reutlingen University [Reu24]).	28
8.1	Thrust vs RPM with quadratic fit: $T = 0.0515 \cdot \text{RPM}^2 - 0.0902 \cdot \text{RPM} - 0.996$ (N). $R^2 = 0.997$	30
8.2	RPM vs Command with linear fit: $\text{RPM} = 19.26 \cdot \text{cmd} + 3.65$ (rev/min). $R^2 = 0.991$	31
8.3	Thrust vs Command showing the direct relationship between motor command and thrust force.	31

List of Tables

5.1	Reynolds numbers for the NACA 0015 wing at various airspeeds with chord length $c = 0.25$ m at sea-level conditions.	14
7.1	Bill of Materials (BOM) for the experimental platform.	27

Bibliography

- [Ca21] F. Chew and et al. *Rapid Design Process of Shrouded Rotors for Efficient UAV Propulsion*. White paper / preprint. 2021.
- [Da24] A. C. Daud Filho and et al. “Transition flight of a concept of lifting-wing vertical takeoff and landing UAV.” In: *The Aeronautical Journal* (2024). doi: 10.1017/aer.2024.100.
- [DD18] D. Dawkins and L. DeVries. “Modeling, Trim Analysis, and Trajectory Tracking Control of a Micro-Quadrotor with Wings.” In: *Drones* 2.2 (2018), p. 21. doi: 10.3390/drones200021.
- [FDF25] A. Freitas, J. Dalmolin, and F. Freitas. “Exploring the Feasibility of Airfoil Integration on Multicopter Arms.” In: *Drones* 9.3 (2025), p. 202. doi: 10.3390/drones9030202.
- [FKa22] P. Foehn, E. Kaufmann, and et al. “Agilicious: Open-source and open-hardware agile quadrotor for vision-based flight.” In: *Science Robotics* 7.67 (2022). doi: 10.1126/scirobotics.abl6259.
- [GLL15] F. A. Goodarzi, T. Lee, and N. H. Lee. “Geometric Adaptive Tracking Control of a Quadrotor UAV on SE(3) for Agile Maneuvers.” In: *ASME Journal of Dynamic Systems, Measurement, and Control* 137.9 (2015). doi: 10.1115/1.4030419.
- [HBC14] V. Hrishikeshavan, J. Black, and I. Chopra. “Design and Performance of a Quad-Shrouded Rotor Micro Air Vehicle.” In: *Journal of the American Helicopter Society / JGCD* (AIAA C-series) (2014). doi: 10.2514/1.C032463.
- [Kam+18] E.-J. van Kampen et al. “Incremental nonlinear dynamic inversion flight control for a fixed-wing UAV.” In: *Journal of Guidance, Control, and Dynamics* (2018).
- [LGa22] G. Lu, H. Guo, and et al. *Trajectory Generation and Tracking Control for Aggressive Tail-Sitter Flights in Unknown Environments*. 2022. arXiv: 2212.11552 [cs.RO].
- [Li+21] Y. Li, Z. Yang, Y. Sun, and J. Wang. “Effect of Ducted Multi-Propeller Configuration on Aerodynamic Performance in Quadrotor Drone.” In: *Drones* 5.3 (2021), p. 101. doi: 10.3390/drones5030101.

Bibliography

- [LLM10] T. Lee, M. Leok, and N. H. McClamroch. “Geometric Tracking Control of a Quadrotor UAV on $\text{SE}(3)$.” In: *49th IEEE Conference on Decision and Control (CDC)*. 2010, pp. 5420–5425. doi: 10.1109/CDC.2010.5717652.
- [MJa22] A. Misra, S. Jayaraman, and et al. “Modeling and Control of a Hybrid Fixed-Wing VTOL-UAV.” In: *International Journal of Intelligent Unmanned Systems* 10 (2022). doi: 10.1155/2022/1803638.
- [MK11] D. Mellinger and V. Kumar. “Minimum Snap Trajectory Generation and Control for Quadrotors.” In: *IEEE International Conference on Robotics and Automation (ICRA)*. 2011, pp. 2520–2525. doi: 10.1109/ICRA.2011.5980409.
- [OŁ22] M. Okulski and M. Ławryńczuk. “A Small UAV Optimized for Efficient Long-Range and VTOL Missions: An Experimental Tandem-Wing Quadplane Drone.” In: *Applied Sciences* 12.14 (2022), p. 7059. doi: 10.3390/app12147059.
- [Oos+17] A. Oosedo et al. “Aerial robot with nimble flight by simplified incremental nonlinear dynamic inversion.” In: *2017 IEEE/RSJ International Conference on Intelligent Robots and Systems (IROS)*. 2017.
- [Per08] J. L. Pereira. *Hover and Wind-Tunnel Testing of Shrouded Rotors for Improved Micro Air Vehicle Design*. PhD Thesis / Technical Report, University of Maryland. 2008.
- [Reu24] Reutlingen University AIDA. *AIDA Hall (Reutlingen University) Photo*. Accessed for facility illustration. 2024. URL: https://aida.reutlingen-university.de/wp-content/uploads/2024/05/20240517_114330-Gros.jpg (visited on 10/12/2025).
- [SCC16] E. Smeur, Q. Chu, and G. C. H. E. de Croon. “Incremental Nonlinear Dynamic Inversion for attitude control of micro air vehicles.” In: *2016 American Control Conference (ACC)*. 2016.
- [SCC17] E. J. J. Smeur, G. C. H. E. de Croon, and Q. P. Chu. *Cascaded Incremental Nonlinear Dynamic Inversion for MAV Disturbance Rejection*. 2017. arXiv: 1701.07254 [cs.R0].
- [SCM10] S. Sieberling, Q. P. Chu, and J. A. Mulder. “Robust Flight Control Using Incremental Nonlinear Dynamic Inversion and Angular Acceleration Prediction.” In: *Journal of Guidance, Control, and Dynamics* 33.6 (2010), pp. 1732–1742. doi: 10.2514/1.49978.
- [Sun+21] S. Sun, A. Romero, P. Foehn, E. Kaufmann, and D. Scaramuzza. *A Comparative Study of Nonlinear MPC and Differential-Flatness-Based Control for Quadrotor Agile Flight*. 2021. arXiv: 2109.01365 [cs.R0].

Bibliography

- [TK18] E. Tal and S. Karaman. *Accurate Tracking of Aggressive Quadrotor Trajectories using INDI and Differential Flatness*. 2018. arXiv: 1809.04048 [cs.R0].
- [TK21a] E. Tal and S. Karaman. “Accurate Tracking of Aggressive Quadrotor Trajectories Using INDI and Differential Flatness.” In: *IEEE Transactions on Control Systems Technology* 29.3 (2021), pp. 1203–1218. doi: 10.1109/TCST.2020.3001117.
- [TK21b] E. Tal and S. Karaman. “Global Trajectory-Tracking Control for a Tailsitter Flying Wing in Agile Uncoordinated Flight.” In: *AIAA Aviation Forum*. 2021, p. 3214. doi: 10.2514/6.2021-3214.
- [TK22] E. Tal and S. Karaman. *Global Incremental Flight Control for Agile Maneuvering of a Tailsitter Flying Wing*. 2022. arXiv: 2207.13218 [cs.R0].
- [Tzo+21] D. Tzoumanikas et al. “High-speed flight in emphagile quadrotors: Incremental Nonlinear Dynamic Inversion for fast and robust tracking.” In: *arXiv preprint arXiv:2109.01365* (2021).
- [XQa20] K. Xiao, Q. Quan, and et al. *A Lifting Wing Fixed on Multirotor UAVs for Long Flight Ranges*. 2020. arXiv: 2006.15579 [cs.R0].